Inorganic Chemistry

Article

pubs.acs.org/IC

Tuning Au(I)···Tl(I) Interactions via Mixed Thia−Aza Macrocyclic Ligands: Effects on the Structural and Luminescence Properties

Rocío Donamaría,[†] Vito Lippolis,*[,‡] José M. López-de-Luzuriaga,*[,†] Miguel Monge,[†] Mattia Nieddu,[†,‡] and M. Elena Olmos*[,†]

[†]Departamento de Química, Universidad de la Rioja, Centro de Investigación en Síntesis Química (CISQ), Complejo Científico Tecnológico, 26004 Logroño, Spain

[‡]Dipartimento di Scienze Chimiche e Geologiche, Università degli Studi di Cagliari, S.S. 554 Bivio per Sestu, 09042 Monserrato, Cagliari, Italy

Supporting Information

ABSTRACT: Reaction of the heterometallic complexes $[\{Au(C_6X_5)_2\}Tl]_n$ (X = Cl, F) with equimolecular amounts of the N,S-mixed-donor crown ethers [12]aneNS$_3$ or [12]aneN$_2$S$_2$ affords the new Au(I)/Tl(I) derivatives $[\{Au(C_6Cl_5)_2\}\{Tl(L)\}_2][Au(C_6Cl_5)_2]$ [L = [12]aneNS$_3$ (**1**), [12]aneN$_2$S$_2$ (**2**)], $[\{Au(C_6F_5)_2\}Tl([12]aneNS_3)]_2$ (**3**), or $[\{Au(C_6F_5)_2\}Tl([12]aneN_2S_2)]_n$ (**4**). These complexes display the same Au/Tl metal ratio, but different structural arrangements. While the chlorinated derivatives **1** and **2**·2THF display an ionic structure, the crystal structure of **3** contains neutral tetranuclear Au_2Tl_2 units, and complex **4** displays a polymeric nature and is the only one that does not show unsupported Au···Tl interactions. The lack of this interaction is responsible for the absence of luminescence in this last case. The optical properties of **1** and **3** in the solid state have been studied experimentally and theoretically, concluding that their luminescence has its origin in the Au···Tl interactions, and this is also influenced by their number and strength. DFT and TD-DFT theoretical calculations on model systems of complexes **1**, **3**, and **4** have been carried out in order to confirm the origin of their luminescence or its absence, as well as to justify their emission energies in spite of their different solid state structures.

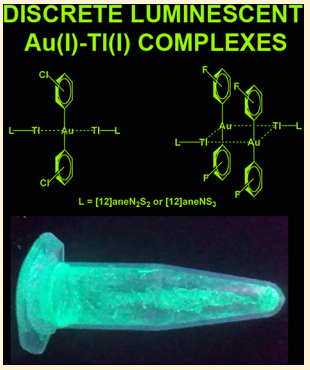

INTRODUCTION

For the last several years, the chemistry of complexes with Au(I)···M (M = closed shell heterometal atom) interactions has been strongly developed. This is mainly due to the interesting chemical and physical properties derived from such interactions, from both a theoretical[1,2] and a practical[3] point of view.

To date, some research groups have invested a lot of effort in studying the origin of the optical properties of these complexes. Thus, it has been established that their luminescence depends on many factors, such as the interacting metals (the nature of the heterometal and the number of interactions present in the complex and their strength), the ligands bonded to the heterometal (the nature of the donor atoms and their behavior as terminal or bridging ligands, which also depends on the number of donor centers and on the size of the ligand), and the coordination environment of the metals. The great number of factors that can affect the optical properties makes the rational design of compounds with a specific luminescence a complex and challenging task.

Our research group has extensive experience in the synthesis of organometallic gold complexes with metal−metal interactions employing an acid−base strategy, developed by our research group years ago, consisting of the reaction of bis(perhalophenylaryl)aurate(I) salts as basic precursors with Lewis acids, such as $AgClO_4$ or $TlPF_6$. Thus, treatment of $NBu_4[Au(C_6X_5)_2]$ (X = F, Cl) with $TlPF_6$ leads to a one-dimensional polymeric complex species, $[\{Au(C_6X_5)_2\}Tl]_n$, with alternating gold and thallium atoms.[4] This complex displays "naked" thallium(I) centers, which allows the incorporation of a variety of electron donor molecules to their coordination sphere. Therefore, depending on the ligand and on the molar ratio employed, complexes displaying structural arrangements that vary from discrete molecules[5,6] to extended networks[7] can be obtained. For example, the use of N-donor ligands such as bipyridine,[7a] triethylenetetramine (trien),[7b] tetramethylenediamine (TMDA),[7b] or 1,10-phenanthroline[7c] affords polymeric compounds that show an emission wavelength above 600 nm. On the other hand, the use of ketones as ligands affords butterfly Au_2Tl_2 clusters whose emission wavelength is more energetic than those corresponding to the polymeric compounds.[5a] Furthermore, the use of crown thioether ligands such as [9]aneS$_3$ (1,4,7-trithiacyclononane) or [14]aneS$_4$ (1,4,8,11-tetrathiacyclotetradecane) affords tetranuclear discrete molecules with a L−Tl−Au−Au−Tl−L disposition in which the crown thioether acts as a terminal ligand, thus preventing polymerization. By contrast, if a larger macrocycle such as [24]aneS$_8$ (1,4,7,10,13,16,19,22-octathiacyclotetracosane) is employed, its behavior as bridging ligand gives rise to an Au−Tl−L−Tl−Au disposition, and affords the formation of polymeric chains as a result of unsupported aurophilic contacts between the Au(I) centers.[5b]

Received: August 8, 2017
Published: September 26, 2017

DOI: 10.1021/acs.inorgchem.7b02035
Inorg. Chem. 2017, 56, 12551−12563

Additionally, in previous works we have established that variations in the basic properties of the gold(I) precursor by changing the halogens present in the aryl group directly affect the characteristics of the final complexes obtained. This is mainly due to the different electronegativity and steric demands of the aryl groups, and hence, different structural and photophysical properties are observed in the final products.[8]

Taking all the above into account, we decided to study the reactivity of the heterometallic compounds $[\{Au(C_6X_5)_2\}Tl]_n$ (X = F, Cl) with 1-aza-4,7,10-trithiacyclododecane ([12]aneNS$_3$) and 1,7-diaza-4,10-dithiacyclododecane ([12]aneN$_2$S$_2$), a couple of macrocyclic ligands with different number of S- and N-donor atoms. These can presumably act as terminal ligands, stabilizing the acid thallium center and avoiding polymerization, thus affording discrete complex species, which presumably display energy emissions near the blue. In addition, by changing the halogen present in the perhalophenyl group bonded to the gold(I) center we could possibly exploit the influence of the basic fragment $[Au(C_6X_5)_2]^-$ to fine-tune the properties of the final products.

RESULTS AND DISCUSSION

Synthesis and Characterization. The heterometallic complexes $[\{Au(C_6Cl_5)_2\}\{Tl(L)\}_2][Au(C_6Cl_5)_2]$ [L = [12]aneNS$_3$ (**1**), [12]aneN$_2$S$_2$ (**2**)], were obtained by reaction of the polymetallic chain compound $[\{Au(C_6Cl_5)_2\}Tl]_n$ with equimolecular amounts of the corresponding N,S-mixed-donor crown ligand ethers in tetrahydrofuran. The substitution of the chlorine atoms in the aryl groups bonded to gold by fluorine does not seem to affect the stoichiometry of the resulting compounds, although their structural disposition and, hence, their optical properties do vary. Thus, the pentafluorophenyl derivatives $[\{Au(C_6F_5)_2\}Tl([12]aneNS_3)]_2$ (**3**) and $[\{Au(C_6F_5)_2\}Tl([12]aneN_2S_2)]_n$ (**4**) were obtained by following the same procedure as for the synthesis of **1** and **2** and using the same molar ratios of the starting products (see Scheme 1). All the complexes are stable to air and moisture for

Scheme 1. Synthesis of Polynuclear Complexes 1−4

$$[Au(C_6Cl_5)_2Tl]_n + L \xrightarrow{THF} [\{Au(C_6Cl_5)_2\}\{Tl(L)\}_2][Au(C_6Cl_5)_2]$$
L=[12]aneNS$_3$(**1**), L=[12]aneN$_2$S$_2$(**2**)

$$[Au(C_6F_5)_2Tl]_n + [12]aneNS_3 \xrightarrow{THF} [\{Au(C_6F_5)\}Tl([12]aneNS_3)]_2\ (3)$$

$$[Au(C_6F_5)_2Tl]_n + [12]aneN_2S_2 \xrightarrow{THF} [\{Au(C_6F_5)\}Tl([12]aneN_2S_2)]_n\ (4)$$

long periods. They are insoluble in dichloromethane, acetonitrile, and diethyl ether, but soluble in O-donor solvents such as tetrahydrofuran or acetone.

Their elemental analyses and spectroscopic data are in accordance with the proposed stoichiometries (see Experimental Section). Their IR spectra display, among others, absorptions arising from the C_6F_5[9] and C_6Cl_5[10] groups bonded to gold(I) at approximately 1500, 950, and 780 cm^{-1}, or about 834 and 614 cm^{-1}, respectively. The presence of the $[Au(C_6F_5)_2]^-$ fragment in **3** and **4** is evident in their ^{19}F NMR spectra, which resemble that of the precursor complex $NBu_4[Au(C_6F_5)_2]$, and seem to indicate that a dissociative process giving rise to aurate(I) anions and thallium(I)-ligand cations takes place in solution.

Regarding the ^{1}H NMR spectra of all complexes in [D$_8$]tetrahydrofuran, they all show the resonances corresponding to the N,S-mixed-donor crown ligand ethers at similar chemical shifts to those found for the free ligands. Therefore, the coordination of the macrocyclic ligands to thallium does not significantly affect the position of the resonances observed in their ^{1}H NMR spectra, nor does the dissociative process affect the N,S-donor molecules. Thus, the ^{1}H NMR spectra of **1** and **3** display two multiplets at 2.72 and 2.91 ppm (**1**) or at 2.77 and 2.98 ppm (**3**), with 1:3 relative integrations, and corresponding to the hydrogen atoms of the methylene groups adjacent to nitrogen or to sulfur, respectively. In the ^{1}H NMR spectra of the other two products, there are two multiplets at 2.81 and 2.98 ppm (**2**) or at 2.89 and 3.05 ppm (**4**), due to the protons of the methylene groups bonded to the N or S atoms of the ring, respectively, and with 1:1 relative integrations.

Regarding their MALDI (−) mass spectra, they display a peak due to the unit $[\{Au(C_6X_5)_2\}_2Tl]^-$ at m/z = 1594 (**1**, **2**) or 1267 (**3**, **4**), and a signal corresponding to $[Au(C_6X_5)_2]^-$ at m/z = 695 (**1**, **2**) or 531 (**3**, **4**) is observed, the latter appearing as parent peak in all the cases. In their MALDI (+) mass spectra, peaks due to the fragment $[Tl(L)]^+$ appear at m/z = 428 (**1**, **3**) or 411 (**2**, **4**), showing experimental isotopic distributions in agreement with the theoretical ones.

Finally, the molar conductivity measurements of the four complexes in acetone agree with a dissociative process in solution, showing values corresponding to uni-univalent electrolytes (see Experimental Section).

Crystal Structures. Single crystals suitable for X-ray diffraction studies were obtained by slow diffusion of *n*-hexane into a saturated solution of the complexes in toluene (complex **1**) or tetrahydrofuran (complexes **2**−**4**). Complex **2** crystallizes with two molecules of THF per molecule of compound. Single-crystal X-ray diffraction has been carried out both at room temperature and at low temperature for compounds **1**, **2**, and **4**. The differences between the structures obtained at different temperatures are negligible. The Au−Tl distances present in compounds **1** and **2** vary from 3.2410(2) (−73 °C) to 3.2514(3) (25 °C) and from 3.3853(5) (−100 °C) to 3.3723(8) (25 °C), respectively. Thus, considering that the structural and thermal parameters at low temperature are better than at room temperature, we have described in detail the former ones. Details of the data collection and refinement are given in Table S1, and selected bond lengths and angles are collected in Tables 1−3.

Although the four crystal structures contain similar structural motifs, $[Au(C_6X_5)_2]^-$ and $[Tl(L)]^+$ units, there are significant differences among them. The crystal structures of **1** and **2**·2THF, with pentachlorophenyl ligands bonded to gold(I), show the same ionic structure, which consists of a trinuclear

Table 1. Selected Bond Lengths [Å] and Angles [deg] for 1[a]

Au(1)−Tl(1)	3.2410(2)	Tl(1)−S(1)	3.0984(13)
Au(1)−C(1)	2.058(5)	Tl(1)−S(2)	3.2018(14)
Au(2)−C(11)	2.045(5)	Tl(1)−S(3)	3.0808(14)
Tl(1)−N(1)	2.724(4)		
C(1)−Au(1)−C(1)#1	180.0	Au(1)−Tl(1)−S(2)	167.17(2)
Tl(1)#1−Au(1)−Tl(1)	180.0	S(1)−Tl(1)−S(3)	109.70(3)
C(11)−Au(2)−C(11)#2	180.0		

[a]Symmetry transformations used to generate equivalent atoms: #1 $-x+1, -y+1, -z$; #2 $-x+1, -y+1, -z+1$.

DOI: 10.1021/acs.inorgchem.7b02035
Inorg. Chem. 2017, 56, 12551−12563

Table 2. Selected Bond Lengths [Å] and Angles [deg] for 2·2THF[a]

Au(1)−Tl(1)	3.3853(5)	Tl(1)−N(2)	2.710(13)
Au(1)−C(1)	2.057(10)	Tl(1)−S(1)	3.110(5)
Au(2)−C(7)	2.041(12)	Tl(1)−S(2)	3.089(5)
Tl(1)−N(1)	2.709(11)		
C(1)#1−Au(1)−C(1)	180.0	Au(1)−Tl(1)− N(2)	158.6(3)
Tl(1)#1−Au(1)−Tl(1)	180.0	S(1)−Tl(1)−S(2)	114.11(12)
C(7)#2−Au(2)−C(7)	180.0		

[a]Symmetry transformations used to generate equivalent atoms: #1 $-x + 2, -y + 2, -z + 1$; #2 $-x, -y, -z$.

Table 3. Selected Bond Lengths [Å] and Angles [deg] for 3[a]

Au(1)−Tl(1)	3.3170(4)	Tl(1)−N(1)	2.767(5)
Au(1)−Tl(1)#1	3.3815(4)	Tl(1)−S(1)	3.1644(15)
Au(1)−C(1)	2.061(5)	Tl(1)−S(2)	3.1569(16)
Au(1)−C(11)	2.055(5)	Tl(1)−S(3)	3.1686(15)
C(11)−Au(1)−C(1)	177.4(2)	S(1)−Tl(1)−S(3)	106.65(4)
Tl(1)−Au(1)−Tl(1)#1	104.27(2)	S(2)−Tl(1)−Au(1)	159.85(3)
Au(1)−Tl(1)−Au(1)#1	75.71(1)	N(1)−Tl(1)−Au(1)#1	171.25(10)

[a]Symmetry transformations used to generate equivalent atoms: #1 $-x + 1, y, -z + 1/2$.

$[\{Au(C_6Cl_5)_2\}\{Tl(L)\}_2]^+$ cation with a novel L−Tl−Au−Tl−L disposition and a $[Au(C_6Cl_5)_2]^-$ fragment as counterion (see Figure 1).

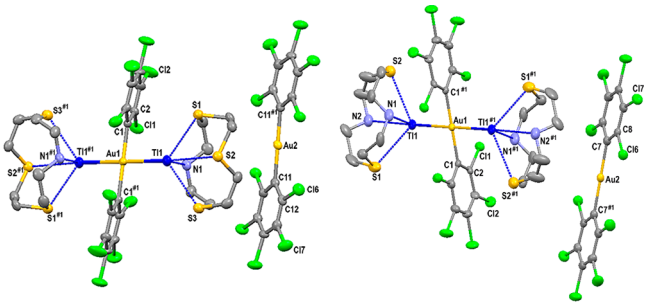

Figure 1. Crystal structures of **1** (left) and **2**·2THF (right) with the labeling scheme for the atom positions. Hydrogen atoms are omitted for clarity, and ellipsoids are drawn at the 30% level. #1 $-x + 1, -y + 1, -z$; #2 $-x + 1, -y + 1, -z + 1$ (**1**). #1 $-x, -y, -z + 1$; #2 $-x, -y, -z$ (**2**·2THF).

The intermetallic distances within the cations are different depending on the macrocyclic ligand employed, showing a Au−Tl distance of 3.2410(2) Å in the [12]aneNS$_3$ derivative **1**, shorter than that of 3.3853(5) Å observed in the [12]aneN$_2$S$_2$ complex **2**·2THF. Nevertheless, both of them lie within the range of Au−Tl distances described to date, which varies from 2.804(6) Å, observed in $[AuPdTl(P_2phen)_3](BF_4)_2 \cdot 2.5CH_2Cl_2$,[11] to 3.4899(6) Å, found in [Tl(2,2′-bipy)][Au(C$_6$F$_5$)$_2$],[7c] and they both are longer than the average Au−Tl distance of 3.064 Å (121 entries in 52 crystal structures in the CCDC). Each gold atom is linearly coordinated to two pentachlorophenyl groups, displaying normal Au−C bond lengths of 2.058(5) and 2.045(5) Å in **1**, and of 2.057(10) and 2.041(12) Å in **2**·2THF.

The Tl−N bond distances are similar in both crystal structures, with values of 2.724(4) Å in **1** and 2.709(11) and 2.710(13) Å in **2**·2THF, and are intermediate between those described for the thallium(I) derivatives with cyclic N- or N,S-donor ligands [Tl(Me$_3$[9]aneN$_3$)]PF$_6$ (2.59(2)−2.63(1) Å)[12] or [Tl([9]aneN$_2$S)][ClO$_4$] (2.26(2)−2.68(2) Å)[13] and [Tl([18]aneN$_2$S$_4$)]PF$_6$ (2.834(4) and 2.992(4) Å).[14] Regarding the Tl−S bonds, in **1** there are two short (3.0808(14) and 3.0984(13) Å) distances and one longer (3.2018(14) Å) distance, the two former nearly equal to those found in **2**·2THF (3.089(5) and 3.110(5) Å), and to those reported for [Tl([9]aneS$_3$)]PF$_6$ (3.092(3)−3.114(3) Å).[15] They all are in general shorter than in the related Au/Tl compounds with crown thioethers $[\{Au(C_6Cl_5)_2\}_2Tl_2([24]aneS_8)]_n$ (3.256(7)−3.587(7) Å), $[\{Au(C_6F_5)_2\}_2Tl_2([24]aneS_8)]$ (3.201(2)−3.418(3) Å), and $[\{Au(C_6F_5)_2\}Tl([9]aneS_3)]_2$ (3.0246(17)−3.1154(19) Å),[5b] as well as in the thallium derivatives [Tl([18]aneN$_2$S$_4$)]PF$_6$ (3.1299(13)−3.4778(15) Å),[14] [Tl([18]aneS$_6$)]PF$_6$ (3.164(5)−3.370(5) Å),[14] and [Tl([24]-aneS$_8$)]PF$_6$ (3.2413(11)−3.4734(14) Å).[14] Only in the case of [Tl([9]aneN$_2$S)][ClO$_4$], which also shows stronger Tl−N bonds, the Tl−S distances are shorter than in these two new complexes, showing values of 2.920(8) and 2.955(7) Å[13] for the latter. In both crystal structures, the lone pair of the thallium centers appears to be stereochemically active, occupying the sixth position of a distorted pseudo-octahedral environment for thallium.

Finally, an extended polymeric structure is formed in both cases via weak intermolecular Tl···Cl contacts of 3.6998(13) Å in **1** and of 3.6597(32) Å in **2**·2THF. The main difference between both unidimensional polymers is the relative position of the chlorine atoms of the aryl groups involved in these interactions: *ortho* in the structure of **1** or *para* in that of **2**·2THF (Figure 2). Additionally, complex **1** also displays a

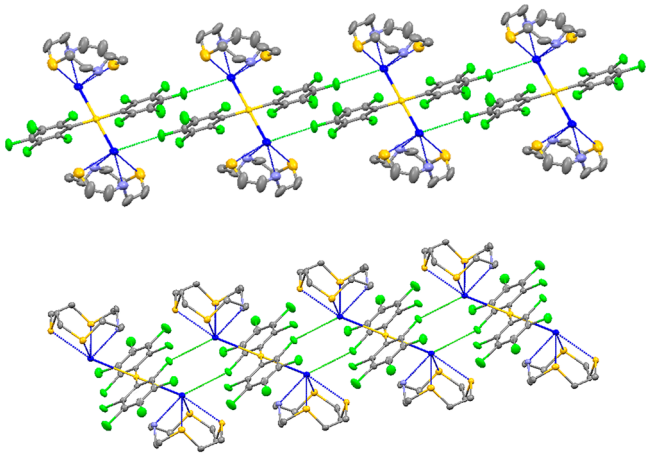

Figure 2. 1D polymeric structures of **1** (top) and **2**·2THF (bottom) formed via Tl···Cl interactions. The counterions have been omitted for clarity.

couple of intramolecular Tl···Cl contacts of 3.4903(14) and 3.6257(14) Å. Figure S1 displays the disposition of the THF molecules in the extended structure of complex **2**.

The substitution of the chlorine by fluorine atoms in the aryl groups bonded to gold leads to significant differences in the crystal structures of complexes **3** and **4**. Thus, the structure of the former consists of a tetranuclear neutral molecule with a central Au$_2$Tl$_2$ core (see Figure 3), similar to the loosely bound butterfly clusters previously described by our research group for some Au(I)/Tl(I) complexes containing O-donor ligands.[5a,16]

DOI: 10.1021/acs.inorgchem.7b02035
Inorg. Chem. 2017, 56, 12551−12563

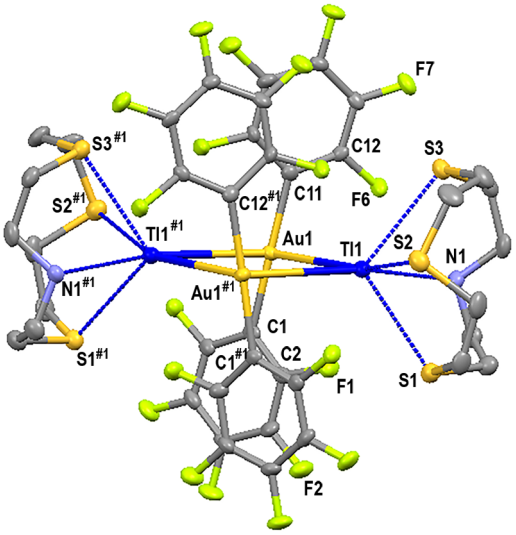

Figure 3. Molecular structure of compound **3** with the labeling scheme for the atom positions. Hydrogen atoms are omitted for clarity, and ellipsoids are drawn at the 30% level. #1 $-x + 1, y, -z + 1/2$.

However, in complex **3** the Au_2Tl_2 unit is planar and no Tl···Tl interaction is observed (Tl−Tl distance of 5.289 Å), while the previously reported structures display a folded core with Tl···Tl contacts between 3.6027(6) Å in $[Au_2Tl_2(C_6Cl_5)_4]\cdot(Me_2CO)$[17] and 3.7152(4) Å in $[Au_2Tl_2(C_6Cl_5)_4]\cdot(acacH)]$.[5a] This disposition of the metals, together with the presence of bulkier ligands at the thallium center, is probably the reason why the Au−Tl distances in the crystal structure of **3** (3.3170(4) and 3.3815(4) Å) are also longer than in the cited compounds, in which the Au−Tl distances lie within the 3.0167(4)−3.2414(3) Å range. Furthermore, neither intra- nor intermolecular aurophilic interactions are observed in **3**, where the minimum Au−Au distance is 4.111 Å.

The gold atoms in the structure of **3** are again linearly coordinated to two aryl groups (C−Au−C = 177.4(2)°), with typical Au−C bond lengths of 2.061(5) and 2.055(5) Å. When the Au···Tl contacts are considered, the square-planar environment observed in **1** and **2**·2THF for the gold centers of the cationic units is now transformed in a seesaw disposition (Tl−Au−Tl = 104.27(2)°) as a consequence of the incorporation of the second bis(aryl)aurate(I) fragment to form the tetranuclear Au_2Tl_2 core.

As observed in Figure 3, the thallium atoms are coordinated to the four donor atoms of the [12]aneNS$_3$ crown ligand and also interact with both gold centers, which results in a distorted octahedral environment for thallium. The Tl−N distance of 2.767(5) Å is shorter than in **1** and **2**·2THF, and it is also intermediate between those found in $[Tl(Me_3[9]aneN_3)]PF_6$ (2.59(2)−2.63(1) Å)[12] or $[Tl([9]aneN_2S)][ClO_4]$ (2.26(2)−2.68(2) Å)[13] and $[Tl([18]aneN_2S_4)]PF_6$ (2.834(4) and 2.992(4) Å).[14] The Tl−S distances in **3** (between 3.1569(16) and 3.1686(15) Å) are also in general longer than in **1** (3.0808(14)−3.2018(14) Å), **2**·2THF (3.089(5) and 3.110(5) Å), and $[\{Au(C_6F_5)_2\}Tl([9]aneS_3)]_2$ (3.0246(17)−3.1154(19) Å),[5b] but shorter than in the related Au(I)/Tl(I) complexes $[\{Au(C_6Cl_5)_2\}_2Tl_2([24]aneS_8)]_n$ (3.256(7)−3.587(7) Å) and $[\{Au(C_6F_5)_2\}_2Tl_2([24]aneS_8)]$ (3.201(2)−3.418(3) Å).[5b]

Finally, the low quality of the crystals of **4**, as well as the high degree of disorder found in the ligand [12]aneN$_2$S$_2$, does not allow us to give bond lengths and angles with adequate accuracy, although a rough description of its structure can be done, and the absence of intermetallic interactions in this case can be definitively confirmed. The crystal structure of **4** can be described as a polymeric chain of alternating $[Au(C_6F_5)_2]^-$ and $[Tl([12]aneN_2S_2)]^+$ units, in which the sulfur atoms of the N,S-mixed-donor crown ether ligand as well as the fluorine atoms in the *ortho* position of the pentafluorophenyl rings act as bridges (Figure 4). This disposition avoids the formation of Au···Tl interactions (Au−Tl = 4.080 Å), present in the crystal structures of **1**, **2**·2THF, and **3**.

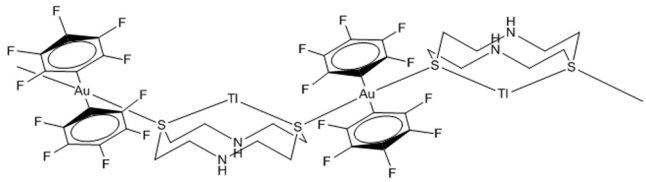

Figure 4. Schematic representation of the 1D polymeric structure of **4**.

Finally, in order to correlate the properties of the bulk solids with the ones obtained from the single crystals used for the X-ray structure determinations, the X-ray powder diffraction spectra were recorded for all complexes (see Figures S2−S5). The experimental diffraction pattern for complexes **1** and **4** matches the theoretical one, while for complex **3** we have observed a partial amorphization, and in the case of complex **2**, the presence of solvent in the crystal structure and its absence in the bulk solid provoke the appearance of a different pattern.

Photophysical Properties. The absorption spectrum of complex **1** shows similar features to those described for other related gold(I)−thallium(I) derivatives reported previously by some of us.[5b] Thus, this complex displays two intense absorptions at about 241 and 292 nm in dilute THF solutions (black profile). These bands are slightly blue-shifted in the spectrum of the heterometallic precursor $[\{Au(C_6Cl_5)_2\}Tl]_n$ (red profile) and in the gold(I) complex $NBu_4[Au(C_6Cl_5)_2]$ (blue profile) (see Figure 5). Therefore, it is likely that the band at high energy arises from transitions between π orbitals of the perhalophenyl groups,[18,3c] which are present in all derivatives. The low energy band observed for **1** and the

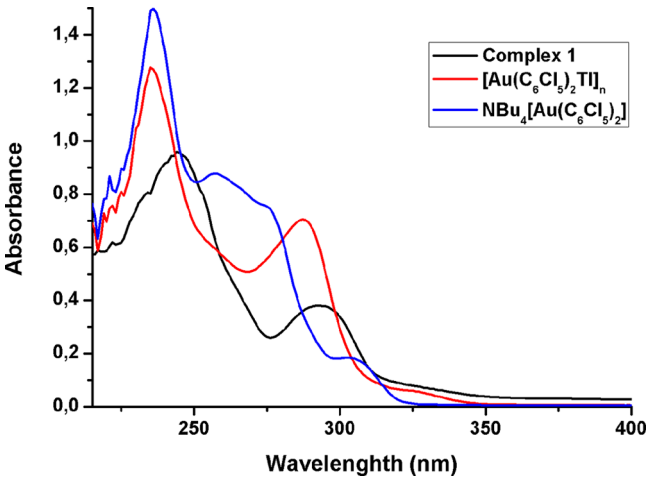

Figure 5. Absorption spectra for complex **1** (3×10^{-5} M) and the gold precursors $NBu_4[Au(C_6F_5)_2]$ (3.5×10^{-5} M) and $[\{Au(C_6F_5)_2\}Tl]_n$ (3.2×10^{-5} M) in dilute THF solutions.

DOI: 10.1021/acs.inorgchem.7b02035
Inorg. Chem. 2017, 56, 12551−12563

heterometallic precursor $[\{Au(C_6Cl_5)_2\}Tl]_n$ could be related to the presence of the Tl(I) center. The red-shift observed for complex **1** would be related to the presence of the thia−aza macrocyclic ligand interacting with the Tl(I) center. Therefore, a MLCT character cannot be ruled out.

Taking into account the different patterns found for the powder X-ray diffraction for complex **2** in the single crystal and bulk solid, we cannot safely associate the photophysical properties of the bulk solid with the crystal structure found. Consequently, all the photophysical and computational discussion on this trinuclear arrangement will be made for complex **1**, assuming that the optical behavior of complex **2** is closely related to it, whose only difference is the terminal macrocyclic ligands that do not participate in the electronic transitions responsible for the emissive behavior (see Computational Studies).

In the case of the pentafluorophenyl derivatives **3** and **4**, the spectra show different profiles as they also display differences in their structures (see X-ray structure discussion). In both cases, the absorptions observed for the precursors $[Au(C_6F_5)_2Tl]_n$ and $NBu_4[Au(C_6F_5)_2]$ appear in the spectra of both complexes, and the assignations can be the same as those made for compound **1**. In addition, a well-defined absorption at 278 nm for complex **4** or a lower energy tail in complex **3** is likely to be due to transitions in which orbitals of the metal centers are involved as, for instance, in charge transfer transitions (see Figure 6). This spectroscopic assignment has been observed in previous studies.[3c]

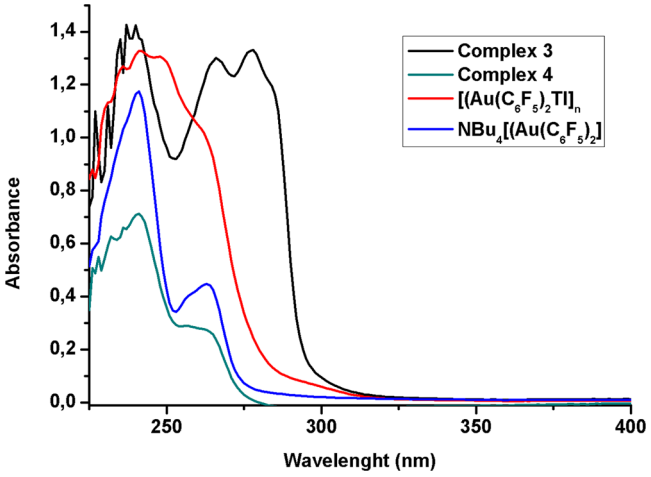

Figure 6. Absorption spectra for complexes **3** (2.2×10^{-5} M) and **4** (2.3×10^{-5} M) and the gold precursors $NBu_4[Au(C_6Cl_5)_2]$ (5×10^{-5} M) and $[\{Au(C_6Cl_5)_2\}]Tl]_n$ (2.7×10^{-5} M) in dilute THF solutions.

As in other compounds displaying heterometallic interactions, complexes **1** and **3** are strongly luminescent in the solid state; nevertheless, complex **4**, in which the intermetallic interactions are absent, does not show any emission, confirming the importance of these interactions in the optical behavior of this type of compounds. Thus, complexes **1** and **3** display emissions in the solid state at 495 nm at room temperature, and at 512 and 475 nm, respectively, when the measurements are carried out at liquid nitrogen temperature (77 K) (Figure 7 and Table 4). We have performed the measurement of the luminescence of complex **1** diluted in KBr. The result shows a less intense emission of the diluted sample, precluding a reabsorption effect (see Figure S6). Both complexes **1** and **3**

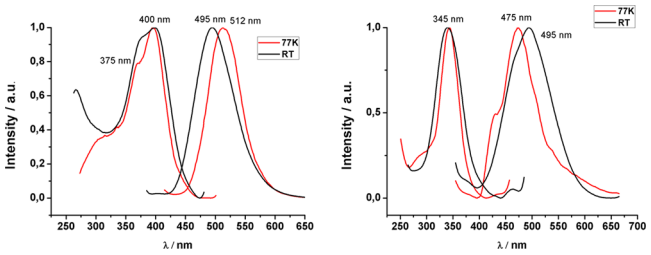

Figure 7. Excitation and emission spectra for complexes **1** (left) and **3** (right) in the solid state at RT and 77 K.

display lifetimes of hundreds of nanoseconds at room temperature. This fact and the large Stokes shifts observed suggest that the emissions probably arise from spin-forbidden transitions. Complexes **1** and **3** undergo an increase in the emission intensity and in the lifetime when decreasing the temperature to 77 K, which suggests that nonradiative decay mostly occurs from the triplet state. The real emission spectra at both temperatures showing the different intensities are included in the Supporting Information (see Figures S7 and S8). This fact allows us to assume that when the excitation of the samples is carried out directly to the triplet state ($\phi_{ISC} = 1$), the radiative rate constant can be approximately estimated for each compound. The k_r values obtained are shown in Table 4. These values found are higher than those usually displayed by other homometallic Au(I) complexes[19] and are comparable to those previously obtained for Au−Cu complexes reported recently by Berger, Monkowius, et al. and with Ir(III)-based emitters.[20] In addition, when the quantum yields are registered with higher energy excitations, hitting the S_1 excited state (320 and 315 nm, respectively), we observe in the case of complex **1** a similar quantum yield and in the case of complex **3** a clear decrease in the quantum yield, suggesting a similar or lower efficiency (more than 50%) of the triplet emission, respectively, and hence, disfavoring the intersystem crossing and the emission from the lowest triplet excited state in the case of **3**. Overall, the spin−orbit coupling (SOC) needed for this triplet emission would arise from the presence of some metal-centered character in the orbitals responsible for the singlet−triplet electronic transition (see Computational Studies) and as a result of the dative anion−cation intermetallic interaction for both complexes **1** and **3**.

The different energies seem to be related to the different structures of the complexes in the solid state, which depend, among other factors, on the N,S-mixed-donor ligand and the perhalophenyl groups bonded to the gold center, and no sign of a unique dependence on the Au−Tl distances is evident. Thus, complex **1**, with the shorter intermetallic distance (3.2410(2) Å), shows the same emission energy at RT as complex **3** (495 nm). The latter, with two different Au−Tl distances (3.3170(4) and 3.3815(4) Å), only displays one emission at this high energy value. In this regard, in gold(I)−thallium(I) complexes whose emissions are metal centered, what it is generally expected is that the shorter the intermetallic interaction, the longer wavelength appears.[2b] It is also curious that in the case of complex **3** the emission at 77 K leads to a higher energy emission, while complex **1** shows the expected emission red-shift. The shift to lower energies when lowering temperature is usually observed in complexes whose emissions arise mostly from metal-centered transitions. The observed hypsochromic shift for complex **3** can be related to a *rigidochromic effect* arising from the rigidity of their structures.[8a,21] Nevertheless,

DOI: 10.1021/acs.inorgchem.7b02035
Inorg. Chem. 2017, 56, 12551−12563

Table 4. Photophysical Properties of Complexes 1 and 3

UV−vis in THF (nm)/(mol^{-1} L cm^{-1})	solid em (exc) RT	solid em (exc) 77 K	τ (ns) RT	τ (ns) 77 K	Φ (λ_{exc} T_1/S_1)	k_r/k_{nr} (s^{-1})
		Complex **1**				
241/(ε = 38333)292/(ε = 17000)	495 (400)	512 (400)	434 ± 3	794 ± 79	2.0/2.0	$4.6 \times 10^4/2.3 \times 10^6$
		Complex **3**				
240/(ε = 64545)266/(ε = 59090) 278/(ε = 60454)	495 (345)	475 (345)	633 ± 13	939 ± 23	5.4/2.2	$9.5 \times 10^4/1.6 \times 10^6$

the contribution from orbitals of the interacting metal centers in the transitions responsible for the optical behavior is evident, since none of the complexes show luminescence in solution either at room temperature or at 77 K. This result is likely to be related to the rupture of the metal−metal interactions promoted by the solvent (see molar conductivity values in the Experimental Section). In addition, complex **4**, in which the Au···Tl interactions are absent, does not show luminescence in the solid state.

Thus, taking into account the previous comments, we can propose that the presence of intermetallic interactions in the solid state, as well as their number and strength, seems to be the key to explain the luminescence of these complexes. Nevertheless, another factor that should be considered is the disposition of these metal centers in the crystal structures, which is determined by the electronic characteristics and the number and type of the donor centers of the thioether-crown ligands.

Finally, the Jablonski diagram (Figure 8) and Table 4 summarize the optical behavior displayed by complexes **1** and **3**. They show that from the singlet−singlet excitation (blue arrow) there is an intersystem crossing, assuming a 100% yield, to a triplet excited state, leading to a phosphorescent emission (green arrow). The observed emission (495 nm for both complexes at RT) is a phosphorescent process in all cases. This triplet excited state can be directly reached via excitation at 400 and 345 nm for complexes **1** and **3**, respectively (see Figure 8).

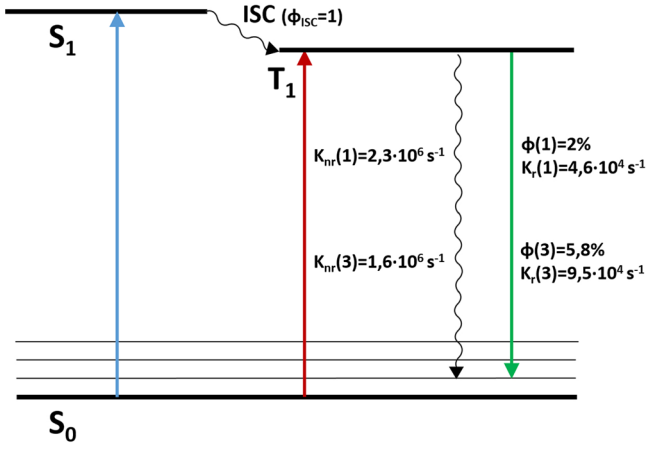

Figure 8. Jablonski diagram for complexes **1** and **3**.

Computational Studies. The assignment of the origin of the luminescence and the justification of the observed emission energies, despite the different structural arrangements found in solid state, is not straightforward. Consequently, additional tools are needed and, for this reason, we carried out density functional theory (DFT) and time-dependent density functional theory (TD-DFT) calculations on model systems **1a**, **3a**, and **4a** of complexes **1**, **3**, and **4**, respectively. The model systems **1a** and **3a** permit analysis of the influence on the photophysical properties of several characteristics of the complexes, such as the different C_6Cl_5 or C_6F_5 perhalophenyl groups bonded to gold(I) in different complexes, their different nuclearities (trinuclear or tetranuclear complexes), or the different metallic arrangements found in their structures (see Figure 9). We have also calculated the electronic structure of model **4a** in order to analyze the lack of luminescent properties for this complex (see Supporting Information).

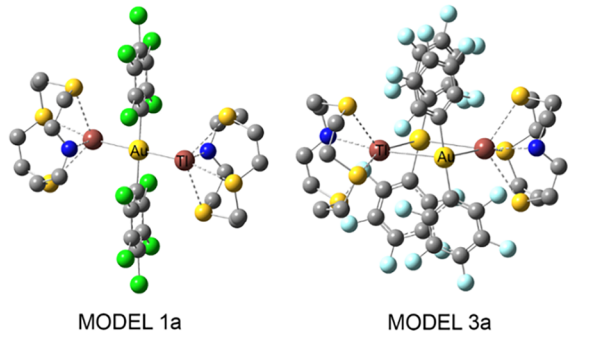

Figure 9. Theoretical model systems $[\{Au(C_6Cl_5)_2\}\{Tl([12]aneNS_3)\}_2]^+$ (**1a**) and $[\{Au(C_6F_5)\}Tl([12]aneNS_3)]_2$ (**3a**).

Thus, model **1a** corresponds to the trinuclear cation found for complex **1**, representing the Au(I)···Tl(I) interactions between one $[Au(C_6Cl_5)_2]^-$ anionic fragment and two cationic $[Tl([12]aneNS_3)]^+$ ones. Meanwhile, model **3a** corresponds to the Au(I)···Tl(I) interaction between two $[Au(C_6F_5)_2]^-$ anionic fragments and two cationic $[Tl([12]aneNS_3)]^+$ ones, leading to a square-like tetranuclear arrangement of the metals.

We first computed the electronic structures for models **1a** and **3a** at the DFT level of theory. Figures 10, 11, S9, and S10 and Table S4 display the most important frontier molecular orbitals (MOs) and the population analysis of those MOs, respectively. From these data we can anticipate the contribution of each part of the molecule to the frontier orbitals.

We have first used the electronic structure results for a deeper analysis of the role of the lone pair on the computed model systems **1a** and **3a**. In order to have a first estimation we computed the natural population analysis at the DFT level model systems **1a** and **3a**. In both cases the Tl lone pair has a main s-character (more than 98%) and the p-character contribution is nearly negligible. In a DFT study by Mudring et al.[22] the authors stated that the s−p hybridization on thallium complexes is not responsible for the stereochemical activity of the lone pair. Instead, these authors reported that, for macrocyclic crown-ether thallium(I) compounds, the inert $6s^2$ pair of electrons becomes stereochemically active when it is forced to be involved in antibonding orbital interactions formed through the 6s/ligand *n*p corresponding atomic orbitals. The existence of such an antibonding orbital produces a structural distortion placing the thallium(I) center out of the macrocyclic

DOI: 10.1021/acs.inorgchem.7b02035
Inorg. Chem. 2017, 56, 12551−12563

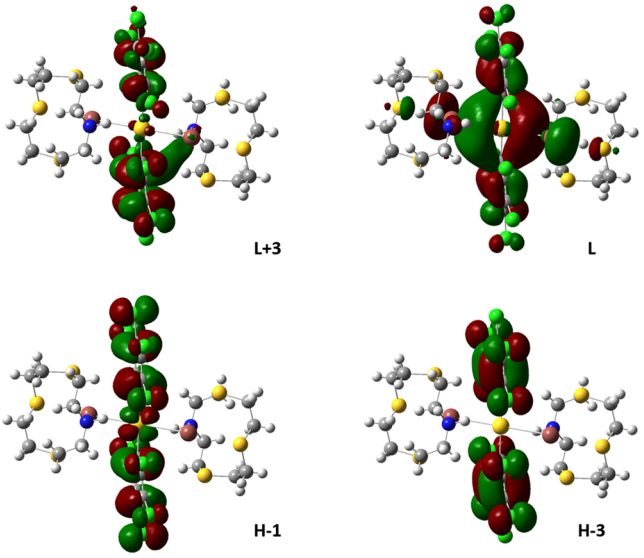

Figure 10. Frontier molecular orbitals (isovalue = 0.02) for model system **1a**.

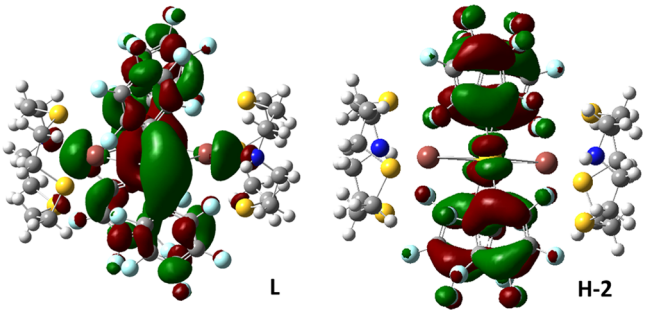

Figure 11. Frontier molecular orbitals (isovalue = 0.02) for model system **3a**.

ligand and, then, makes the lone pair stereochemically active. In the case of the reported complexes we observe different metallic arrangements. Thus, the computed electronic structure for the cationic trinuclear arrangement (model **1a**) observed for complexes **1** and **2** shows a clear antibonding character in the HOMO orbital (see Supporting Information) analogous to the one reported by Mudring et al.,[22] and then, the lone pair is stereochemically active. Indeed, the part of the HOMO orbital located at the Tl(I) center occupies the sixth position of a distorted pseudo-octahedral environment for thallium. We think that the Tl···Cl contacts observed in the crystal structures would be too weak to be considered as coordination positions at Tl(I) centers. In the case of model **3a**, the HOMO orbital (see Supporting Information) also displays the antibonding character and the structural distortion of the Tl center out of the macrocycle, leading to a stereochemically active lone pair for thallium placed between the Tl(I) and Au(I) centers. Also, the acidic character of the Tl(I) center has been analyzed through NBO charge density calculations of model **1a** and on a model system of complex **1** (model **1b**) including the Tl···Cl contacts found experimentally. The results are included Figure S11 and show that the Tl(I) centers are acidic for both model systems, displaying similar charges. The charge on the Tl(I) center interacting with Cl atoms is slightly lower (+0.539) in model **1b** than the charge on the same Tl(I) center (+0.572) without Tl···Cl contacts, which could be in agreement with the existence of these Tl···Cl contacts but as very weak interactions imposed by the 3D-packing.

In the case of the trinuclear cationic complex $[\{Au(C_6Cl_5)_2\}\{Tl([12]aneNS_3)\}_2]^+$ **1a**, the highest occupied molecular orbital (HOMO) and the lowest empty molecular orbital (LUMO) are mainly localized at the metal centers Au(I) and Tl(I). The rest of the occupied and empty frontier molecular orbitals from HOMO−1 to HOMO−9 and from LUMO+1 to LUMO+6 are mostly located at the $[12]aneNS_3$ and C_6Cl_5 ligands, the contribution of the pentachlorophenyl groups being important in the lower empty orbitals from LUMO+1 to LUMO+6.

Model $[\{Au(C_6F_5)\}\{Tl([12]aneNS_3)\}]_2$ **3a** shows common features with the previous model but also some differences. Both the HOMO and LUMO orbitals are, again, mainly located at the metal centers. Lower energy occupied orbitals display a mixed metal/ligand character with a higher contribution from both $[12]aneNS_3$ and C_6F_5 ligands. In contrast to model **1a**, the higher empty MOs from LUMO+1 to LUMO+8 display a predominant Au−Tl character for model system **3a**.

The first 20 singlet−singlet excitations were computed for all model systems at the TD-DFT level of theory as described in Computational Details and compared with the experimental absorption and excitation spectra for complexes **1** and **3** in the solid state. From an experimental point of view, the low intensity region of the absorption spectrum at low energy matches the maximum of the excitation spectrum in the solid state for both emissive compounds (see Figure 12), which is in accordance with the forbidden nature of the electronic excitation responsible for the phosphorescent behavior that these complexes display. Therefore, since the lifetimes for these complexes lie in the microsecond range and they display large Stokes shifts, suggesting phosphorescent processes, we also computed the lowest singlet−triplet excitation at the TD-DFT level for model systems **1a** and **3a**. The results including the most important excitations are depicted in Tables 5 and 6 and Figure 12.

The most intense TD-DFT singlet−singlet excitations for model $[Au(C_6Cl_5)_2Tl([12]aneNS_3)]$ **1a** appear between 234.9 and 320.9 nm, whereas the lowest singlet−triplet excitation appears at 412.0 nm. These values are in agreement with the experimental excitation spectrum for complex **1** for the singlet−triplet transition, which shows a maximum at 400 nm, and with the UV−vis absorption spectrum in the solid state for the allowed singlet−singlet transitions.

If we analyze the TD-DFT results for model **1a**, we can observe that the main contribution of the most intense computed singlet−singlet electronic transition at 321 nm arises from a HOMO−LUMO transition. From the population analysis results (see Table S4), this excitation can be attributed to a metal-centered transition between the interacting Au−Tl centers with a small charge transfer contribution from the $[12]aneNS_3$ ligand to the C_6Cl_5 one. Other intense singlet−singlet excitations at higher energy (between 285.7 to 257.6 nm) consist of transitions between ligand-based orbitals (HOMO−1, HOMO−4, HOMO−5, and HOMO−8) and the metal-based LUMO orbital. The highest energy singlet−singlet transitions (between 255.0 and 234.9 nm) display a mixed character with predominant ligand contributions. The lowest computed singlet−triplet excitation is mainly due to a HOMO−1 to LUMO transition, which can be related to the phosphorescent process found experimentally and attributed to

DOI: 10.1021/acs.inorgchem.7b02035
Inorg. Chem. 2017, 56, 12551−12563

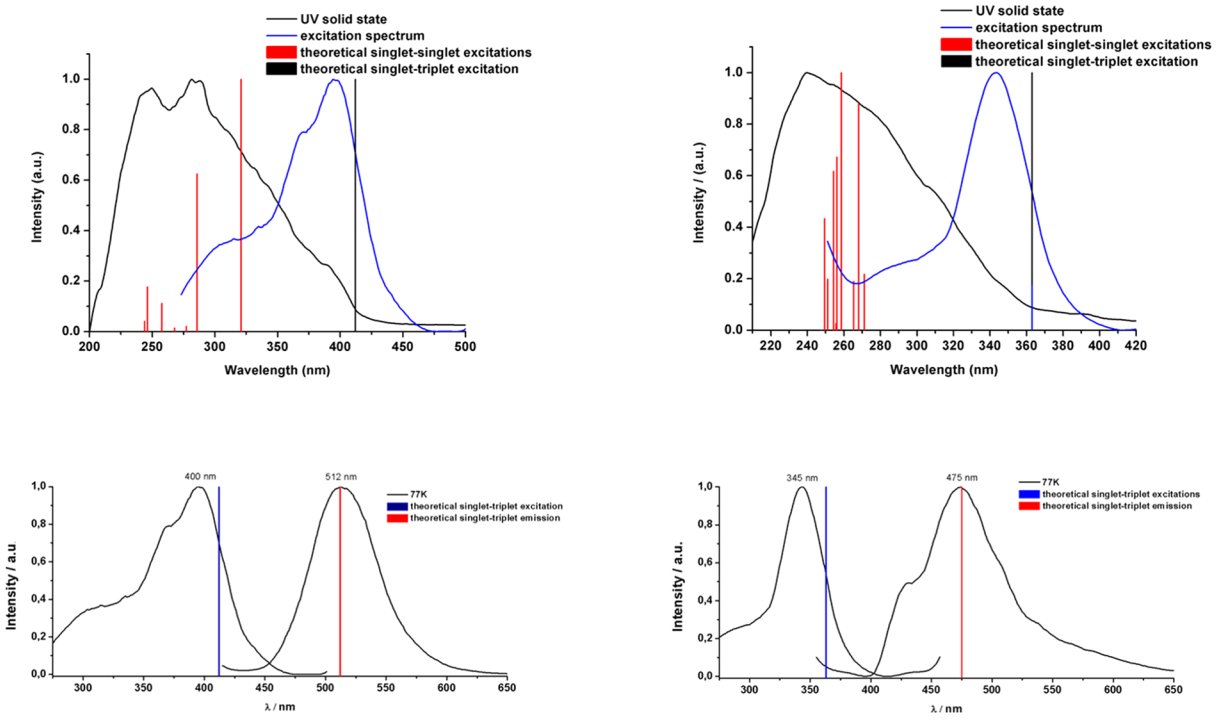

Figure 12. Top: Experimental UV−vis solid state absorption spectrum (black line) and TD-DFT singlet−singlet excitations (red bars) for model systems **1a** (left) and **3a** (right). Bottom: Excitation and emission spectra at 77 K (black profile) and TD-DFT predicted singlet−triplet excitation (blue bar) and triplet−singlet emission (red bar) for model systems **1a** (left) and **3a** (right).

Table 5. TD-DFT First Singlet−Singlet Excitation Calculations and Lowest Singlet−Triplet Excitations for Model System 1a

exc	λ_{calc} (nm)	f (s)	contributions
$S_0 \rightarrow S_1$	320.9	0.4016	HOMO → LUMO (97.4)
$S_0 \rightarrow S_2$	285.7	0.2550	HOMO(−1) → LUMO (96.5)
$S_0 \rightarrow S_5$	277.3	0.0189	HOMO(−5) → LUMO (49.6)
			HOMO(−4) → LUMO (24.6)
$S_0 \rightarrow S_9$	267.8	0.0164	HOMO(−8) → LUMO (16.9)
			HOMO(−5) → LUMO (23.8)
			HOMO(−4) → LUMO (53.3)
$S_0 \rightarrow S_{12}$	257.6	0.0546	HOMO(−8) → LUMO (68.2)
$S_0 \rightarrow S_{14}$	255.0	0.0109	HOMO(−3) → LUMO(+1) (59.8)
$S_0 \rightarrow S_{18}$	246.1	0.0800	HOMO → LUMO(+5) (22.2)
			HOMO → LUMO(+6) (47.0)
$S_0 \rightarrow S_{20}$	234.9	0.0270	HOMO(−9) → LUMO (23.0)
			HOMO(−2) → LUMO(+1) (37.1)
$S_0 \rightarrow T_1$	412.0	0.0000	HOMO(−3) → LUMO(+3) (15.5)
			HOMO(−1) → LUMO (34.0)

Table 6. TD-DFT First Singlet−Singlet Excitation Calculations and Lowest Singlet−Triplet Excitations for Model System 3a

exc	λ_{calc} (nm)	f (s)	contributions
$S_0 \rightarrow S_1$	311.0	0.0012	HOMO → LUMO (68.8)
			HOMO → LUMO+1 (13.5)
$S_0 \rightarrow S_2$	301.3	0.0032	HOMO → LUMO (13.6)
			HOMO → LUMO+1 (67.0)
			HOMO → LUMO+3 (14.5)
$S_0 \rightarrow S_3$	271.1	0.0363	HOMO → LUMO(+2) (93.3)
$S_0 \rightarrow S_5$	268.0	0.1132	HOMO(−1) → LUMO (22.9)
			HOMO → LUMO(+4) (54.2)
$S_0 \rightarrow S_6$	265.3	0.0331	HOMO(−1) → LUMO (71.1)
			HOMO → LUMO(+4) (15.1)
$S_0 \rightarrow S_7$	258.7	0.1272	HOMO → LUMO(+6) (42.6)
			HOMO → LUMO(+8) (39.4)
$S_0 \rightarrow S_9$	256.1	0.0892	HOMO(−2) → LUMO (68.1)
			HOMO → LUMO(+7) (13.6)
$S_0 \rightarrow S_{10}$	255.7	0.0142	HOMO(−3) → LUMO (29.1)
			HOMO(−1) → LUMO(+1) (35.4)
			HOMO → LUMO(+8) (14.3)
$S_0 \rightarrow S_{11}$	254.4	0.0796	HOMO(−3) → LUMO (17.0)
			HOMO(−1) → LUMO(+1) (16.2)
			HOMO → LUMO(+7) (36.2)
$S_0 \rightarrow S_{15}$	251.1	0.0341	HOMO(−4) → LUMO (55.7)
			HOMO(−3) → LUMO (12.3)
$S_0 \rightarrow S_{16}$	249.5	0.0615	HOMO(−8) → LUMO (15.4)
			HOMO(−5) → LUMO (51.1)
$S_0 \rightarrow S_{17}$	247.5	0.0112	HOMO(−2) → LUMO(+1) (85.6)
$S_0 \rightarrow S_{19}$	245.5	0.0111	HOMO(−7) → LUMO (51.2)
$S_0 \rightarrow T_1$	363.0	0.0000	HOMO(−2) → LUMO (17.3)

a charge transfer from the $[Au(C_6Cl_5)_2]^-$ unit to the interacting Au−Tl metal centers.

Model $[\{Au(C_6F_5)\}Tl([12]aneNS_3)]_2$ (**3a**) displays the most intense TD-DFT computed singlet−singlet excitations between 245.5 and 271.1 nm, whereas the lowest singlet−triplet excitation appears at 363.0 nm. These values are in fairly good agreement with the experimental absorption spectrum in the solid state, which shows a maximum at 240 nm and a low energy shoulder at ca. 326 nm for the singlet−singlet transitions and with the excitation spectrum that shows a maximum at 345 nm. The main contribution of the most intense singlet−singlet electronic excitation computed at 258.7 nm is due to two transitions between HOMO−LUMO+6 and HOMO−LUMO

DOI: 10.1021/acs.inorgchem.7b02035
Inorg. Chem. 2017, 56, 12551−12563

+8. Taking into account the character of these orbitals, this transition can be attributed to a metal-centered transition between the interacting Au−Tl centers with a small charge transfer contribution from the [12]aneNS$_3$ ligand to the metals. Other intense singlet−singlet excitations at lower energy, between 271.1 and 265.3 nm, take place between metal-based orbital (HOMO) or mixed orbital (HOMO−1) and the metal-based LUMO, LUMO+2, and LUMO+4 orbitals. The high energy singlet−singlet excitations (from 256.1 to 245.5 nm) can be mainly attributed to arise from charge transfer transitions between mixed ligand−metal or ligand based orbitals (HOMO to HOMO−7) and metal-based orbitals (mainly LUMO and LUMO+7). Finally, the computed lowest singlet−triplet excitation, which is responsible for the phosphorescent character of the emission for complex **3**, is mainly due to a HOMO−2 to LUMO transition. Taking into account the character of these orbitals, this transition can be attributed to a metal-centered transition between the interacting Au−Tl centers with a minor charge transfer contribution from the [12]aneNS$_3$ and C_6F_5 ligands to the metals.

We have carried out a similar DFT analysis for model **4a** (see Figure S12). In this case, the character of the frontier orbitals is different from that obtained for models **1a** and **3a**. Regarding the analysis of the lone pair for Tl(I), the HOMO−2 orbital for model system **4a** also shows the expected antibonding character between the Tl(I) center and the macrocyclic ligand, leading to the stereochemically active lone pair for thallium. On the other hand, the lack of luminescence for complex **4** would arise from the absence of Au(I)···Tl(I) interactions in the molecule, which appear as a very important contribution to the frontier MOs involved in the electronic transitions responsible for the luminescent properties displayed by complexes **1** and **3**. In the case of complex **4**, the frontier orbitals are not a result of the intermetallic interaction between the metals.

In order to assign the origin of the emission found experimentally for complexes **1** and **3**, we computed the optimization of the ground state (S_0) and the lowest triplet excited state (T_1) from which the phosphorescent emission takes place, for model systems of complexes **1** and **3**, i.e., models **1b** and **3b**.

This type of theoretical approach allows us to analyze the most important molecular distortions of the models when changing from the ground to the lowest triplet excited state, that can be related to the part of the molecules involved in the phosphorescent properties. In a second step, we can also analyze the shape of the frontier orbitals for the S_0 and T_1 structures, which would confirm the parts of the molecule involved in the electronic transition (SOMO−SOMO−1) responsible for the phosphorescent behavior of these systems.

Regarding the structural distortions, Figure 13 and Table 7 display the most important optimized distances for models **1b** and **3b** in the ground state S_0 and T_1 excited state. First of all, it is worth mentioning that the optimized structures in the S_0 state for models **1b** and **3b** agree well with the experimental X-ray diffraction data as it can be observed in the intermetallic Au−Tl distances, metal−ligand bonds, and internal C−C, N−C, and S−C distances. If we analyze the main distortion of model systems **1b** and **3b** in the T_1 excited state, there is a clear shortening of the intermetallic Au(I)−Tl(I) distances ranging from 3.189 to 3.202 Å (S_0) to 2.832 Å (T_1) for model **1b** and from 3.249 to 3.407 Å (S_0) to 2.891−3.016 Å (T_1) in the case of model **3b**, leading to intermetallic distance contractions of

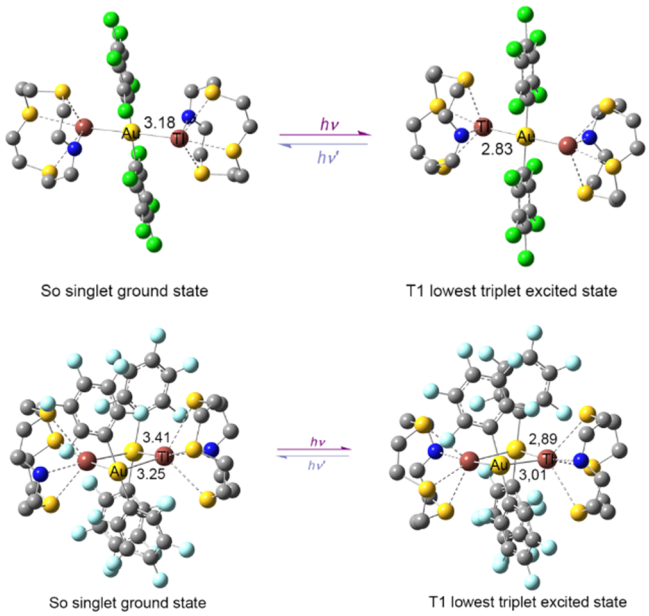

Figure 13. Optimized structures of the ground and lowest triplet excited states for models **1b** (top) and **3b** (bottom).

ca. 11% for both model systems. These intermetallic distance shortenings suggest a main role of the closed shell Au···Tl interaction in the phosphorescent properties of the complexes. A secondary distortion found for both model systems when going from the S_0 to the T_1 excited state is a slight decrease of the Tl−N and Tl−S distances, which suggests a minor role of the [12]aneNS$_3$ ligand in the emissive behavior of complexes **1** and **3**.

The analysis of the shape of the frontier molecular orbitals (Figure 14) of the lowest triplet excited state T_1 (SOMO and SOMO−1) shows, for both models, that the Au−Tl interacting metals are mainly involved in the phosphorescent emission from the T1 state (SOMO−SOMO−1 transition), with some contribution from the ligands. If we compare the shape of SOMO and SOMO−1 orbitals for models **1b** and **3b**, we can also confirm a small charge transfer contribution from the metals to the [12]aneNS$_3$ ligands. Therefore, in view of the analysis of the molecular distortions and the electronic structure of the frontier orbitals of the T_1 state for models **1b** and **3b**, we can conclude that the phosphorescent emission process can be ascribed to a forbidden metal centered (Au−Tl) transition with a small metal (Au−Tl) to ligand ([12]aneNS$_3$) charge transfer contribution. The low intensity region of the absorption spectrum matches the maximum of the excitation spectrum in the solid state for all emissive compounds (see Figure 12), which is in accordance with the forbidden nature of the electronic excitation responsible for the phosphorescent behavior that these complexes display.

Finally, in order to confirm the accuracy of our computational approach, we have computed the emission energies for models **1b** and **3b** as the difference between the energy of the T_1 optimized structures and the same structure in the S_0 ground state. The computed emissions clearly match the experimental ones (495 nm at RT and 512 nm at 77 K exp vs 512 nm theor (**1b**); 495 nm at RT and 475 nm at 77 K exp vs 475 nm theor (**3b**)) confirmed by the calculated theoretical emissions that perfectly match the experimental data.

DOI: 10.1021/acs.inorgchem.7b02035
Inorg. Chem. 2017, 56, 12551−12563

Table 7. Selected Structural Parameters for Complexes 1 and 3 and the Corresponding Model Systems in the Ground (S_0) and the Lowest Triplet Excited State (T_1), at the DFT Level of Theory[a]

	Au−Tl	Au−C	Tl−E	C−Au−C	Tl−Au−Tl	C−C	C−E
1	3.241	2.058	2.725	180.0	180.0	1.379−1.402	1.475−1.482
		2.045	3.081−3.202				1.810−1.821
1b S_0	3.189−3.202	2.067−2.069	2.819	179.5	178.4	1.410−1.414	1.460−1.464
			3.174−3.204				1.830−1.841
1b T_1	2.832	2.061	2.750	180.0	180.0	1.405−1.419	1.459−1.461
			3.049−3.169				1.830−1.842
3	3.317−3.382	2.061	2.772	177.4	104.3	1.369−1.395	1.493−1.496
		2.055	3.156−3.169				1.814−1.842
3b S_0	3.249−3.407	2.064−2.068	2.945	178.8	75.4	1.399−1.404	1.457−1.460
			3.192−3.300				1.829−1.841
3b T_1	2.891−3.016	2.065−2.075	2.951−2.953	171.4	89.6	1.399−1.406	1.450−1.452
			3.104−3.270				1.829−1.840

[a]Distances are in angstroms (Å); angles are in degrees.

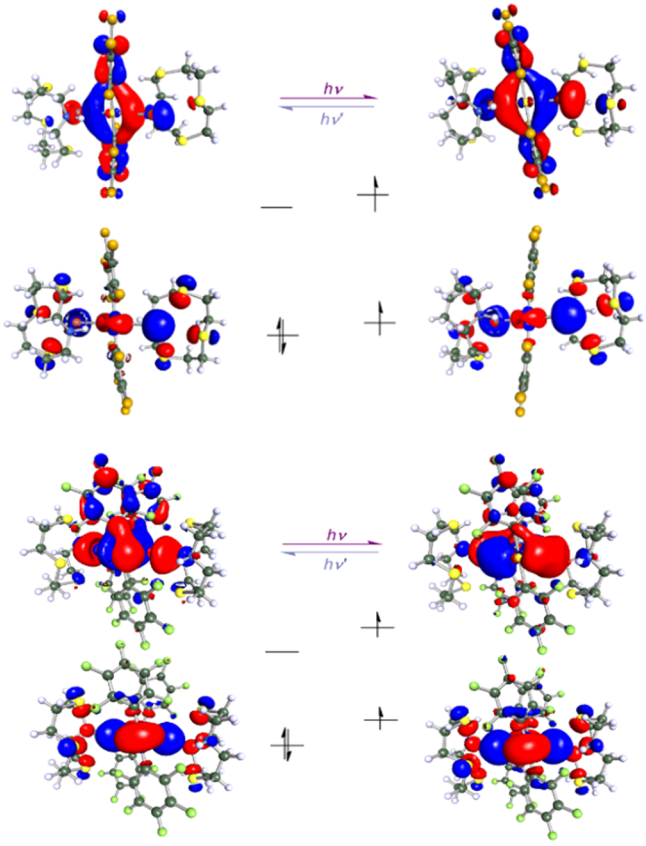

Figure 14. Frontier molecular orbitals HOMO−LUMO (left) and SOMO−SOMO−1 (right) diagrams for models **1a** (up) and **3a** (bottom).

CONCLUSIONS

The use of macrocyclic binder ligands allows generation of luminescent systems containing different metallophilic interactions displaying unprecedented structural arrangements, such as the $[Tl(I)\cdots Au(I)\cdots Tl(I)]^+$ trinuclear disposition observed for complexes **1** and **2** and the Au_2Tl_2 square arrangement for complex **3**. Luminescent properties are directly correlated to the Au(I)−Tl(I) arrangements more than the distances found in the complexes. The computational studies show that the luminescent properties mainly arise from the metals, whereas the macrocyclic ligands serve as a support for the whole structural system, tuning the luminescence as a consequence of the types of Au(I)···Tl(I) interactions. These results are confirmed by the calculated theoretical emissions that perfectly match the experimental data.

EXPERIMENTAL SECTION

General. The N,S-mixed-donor ligands 1-aza-4,7,10-trithiacyclododecane ([12]aneNS$_3$)[23] and 1,7-diaza-4,10-dithiacyclododecane ([12]aneN$_2$S$_2$),[24] and the starting products $[\{Au(C_6Cl_5)_2\}Tl]_n$[3b] and $[\{Au(C_6F_5)_2\}Tl]_n$[4] were prepared according to the literature.

Instrumentation. Infrared spectra were recorded in the 4000−500 cm^{-1} range on a PerkinElmer FT-IR Spectrum Two with an ATR accessory. C, H, and S analyses were carried out with a PerkinElmer 240C microanalyzer. Mass spectra were recorded with a Bruker Microflex MALDI-TOF using dithranol (DIT) or 11-dicyano-4-*tert*-butylphenyl-3-methylbutadiene (DCTB) as the matrix. ^{1}H and ^{19}F NMR spectra were recorded with a Bruker Avance 400 in [D$_8$]tetrahydrofuran. Chemical shifts are quoted relative to SiMe$_4$ (^{1}H, external) and CFCl$_3$ (^{19}F, external). Absorption spectra in solution were recorded on a Hewlett-Packard 8453 diode array UV−vis spectrophotometer. Diffuse reflectance UV−vis spectra of pressed powder samples diluted with KBr were recorded on a Shimadzu (UV-3600 spectrophotometer with a Harrick Praying Mantis accessory) and recalculated following the Kubelka−Munk function. Excitation and emission spectra in the solid state were recorded with a Jobin-Yvon Horiba Fluorolog 3-22 Tau-3 spectrofluorimeter. Lifetime measurements were recorded with a Datastation HUB-B with a nanoLED controller and DAS6 software. The nanoLED employed for lifetime measurements was one of 370 nm with pulse lengths of 0.8−1.4 ns. The lifetime data were fitted with the Jobin-Yvon software package. Quantum yields were measured in solid using the Hamamatsu Absolute PL Quantum Yield Measurement System C11347-11.

Synthesis. *$[\{Au(C_6Cl_5)_2\}\{Tl([12]aneNS_3)\}_2][Au(C_6Cl_5)_2]$ (**1**).* [12]aneNS$_3$ (12.2 mg, 0.055 mmol) was added to a solution of $[\{Au(C_6Cl_5)_2\}Tl]_n$ (50.0 mg, 0.055 mmol) in tetrahydrofuran. The mixture was stirred at room temperature for 3 h, and then the solvent was partially removed under reduced pressure. Finally, the addition of *n*-hexane led to the precipitation of product **1** as a white solid, which was filtered and washed with *n*-hexane (42.0 mg, 68% yield). Elemental analysis (%) calcd for $C_{20}H_{17}AuCl_{10}NS_3Tl$ (1123.43): C 21.38, H 1.53, N 1.25, S 18.19. Found: C 21.00, H 1.73, N 1.39, S 18.22. ^{1}H NMR (400 MHz, [D$_8$]tetrahydrofuran, ppm): δ 2.72 (m, 4H, N−CH_2), 2.91 (m, 12H, S−CH_2). MALDI-TOF(−) *m*/*z* (%): 695 $[Au(C_6Cl_5)_2]^-$ (100), 1594 $[\{Au(C_6Cl_5)_2\}_2Tl]^-$ (42). MALDI-TOF(+) *m*/*z* (%): 428 $[Tl([12]aneNS_3)]^+$ (100). ATR: ν([Au(C$_6$Cl$_5$)$_2$]$^-$) at 834 and 615 cm^{-1}. Λ_M (acetone): 110 Ω^{-1}cm^2 mol^{-1}.

*$[\{Au(C_6Cl_5)_2\}\{Tl([12]aneN_2S_2)\}_2][Au(C_6Cl_5)_2]$ (**2**).* [12]aneN$_2$S$_2$ (11.4 mg, 0.055 mmol) was added to a solution of $[\{Au(C_6Cl_5)_2\}Tl]_n$ (50.0 mg, 0.055 mmol) in tetrahydrofuran. The mixture was stirred at room

DOI: 10.1021/acs.inorgchem.7b02035
Inorg. Chem. 2017, 56, 12551−12563

temperature for 3 h, and then the solvent was partially removed under reduced pressure. Finally, the addition of *n*-hexane led to the precipitation of product **2** as a gray solid, which was filtered and washed with *n*-hexane (43.2 mg, 70% yield). Elemental analysis (%) calcd for $C_{20}H_{18}AuCl_{10}N_2S_2Tl$ (1106.52): C 21.71, H 1.64, N 2.53, S 5.80. Found: C 21.87, H 1.74, N 2.21, S 5.55. ^{1}H NMR (400 MHz, [D_8]tetrahydrofuran, ppm): δ 2.81 (m, 8H, N−CH_2), 2.98 (m, 8H, S−CH_2). MALDI-TOF(−) *m*/*z* (%): 695 [$Au(C_6Cl_5)_2]^-$ (100), 1594 [$\{Au(C_6Cl_5)_2\}_2Tl]^-$ (25). MALDI-TOF(+) *m*/*z* (%): 411 [Tl([12]-aneN$_2$S$_2$)]$^+$ (100). ATR: ν([$Au(C_6Cl_5)_2]^-$) at 838 and 615 cm^{-1}. Λ_M (acetone): 115 Ω^{-1} cm^2 mol^{-1}.

[{Au(C$_6$F$_5$)$_2$}Tl([12]aneNS$_3$)]$_2$ (**3**). To a well stirred solution of [$\{Au(C_6F_5)_2\}Tl]_n$ (50 mg, 0.068 mmol) in tetrahydrofuran, [12]-aneNS$_3$ (15,5 mg, 0.068 mmol) was added. After 2 h of stirring, the solution was concentrated under vacuum. Finally, the addition of *n*-hexane led to the precipitation of product **3** as a white solid, which was filtered and washed with *n*-hexane (42.3 mg, 65% yield). Elemental analysis (%) calcd for $C_{20}H_{17}AuF_{10}NS_3Tl$ (958.88): C 25.05, H 1.79, N 1.46, S 10.03. Found: C 25.31, H 1.88, N 1.53, S 10.33. ^{1}H NMR (400 MHz, [D_8]tetrahydrofuran, ppm): δ 2.77 (m, 4H, N−CH_2), 2.98 (m, 12H, S−CH_2). ^{19}F NMR (400 MHz, [D_8]tetrahydrofuran, ppm): δ −117.1 (m, 2F, F_o), −166.0 (t, 1F, F_p, $^3J(F_p-F_m)$ = 19.3 Hz), −167.3 (m, 2F, F_m). MALDI-TOF(−) *m*/*z* (%): 531 [$Au(C_6F_5)_2]^-$ (100), 1267 [$\{Au(C_6F_5)_2\}_2Tl]^-$ (30). MALDI-TOF(+) *m*/*z* (%): 428 [Tl([12]aneNS$_3$)]$^+$ (30). ATR: ν([$Au(C_6F_5)_2]^-$) at 1502, 952, and 785 cm^{-1}. Λ_M (acetone): 102 Ω^{-1} cm^2 mol^{-1}.

[{Au(C$_6$F$_5$)$_2$}Tl([12]aneN$_2$S$_2$)]$_n$ (**4**). To a well stirred solution of [$\{Au(C_6F_5)_2\}Tl]_n$ (50 mg, 0.068 mmol) in tetrahydrofuran, [12]-aneN$_2$S$_2$ (14.0 mg, 0.068 mmol) was added. After 2 h of stirring, the solution was concentrated under vacuum. Finally, the addition of *n*-hexane led to the precipitation of product **4** as a gray solid, which was filtered and washed with *n*-hexane (42.0 mg, 65% yield). Elemental analysis (%) calcd for $C_{20}H_{17}AuF_{10}N_2S_2Tl$ (942.01): C 25.50, H 1.93, N 2.97, S 6.81. Found: C 25.35, H 2.01, N 2.90, S 6.72. ^{1}H NMR (400 MHz, [D_8]tetrahydrofuran, ppm): δ 2.89 (m, 8H, N−CH_2), 3.05 (m, 18H, S−CH_2). ^{19}F NMR (400 MHz, [D_8]tetrahydrofuran, ppm): δ −115.21 (m, 2F, F_o), −164.7 (t, 1F, F_p, $^3J(F_p-F_m)$ = 18.6 Hz), −165.3 (m, 2F, F_m). MALDI-TOF(−) *m*/*z* (%): 531 [$Au(C_6F_5)_2]^-$ (100), 1267 [$\{Au(C_6F_5)_2\}_2Tl]^-$ (10). MALDI-TOF(+) *m*/*z* (%): 411 [Tl([12]aneN$_2$S$_2$)]$^+$ (10). ATR: ν([$Au(C_6F_5)_2]^-$) at 1508, 957, and 784 cm^{-1}. Λ_M (acetone): 120 Ω^{-1} cm^2 mol^{-1}.

Crystallography. Crystals were mounted in inert oil on glass fibers and transferred to the cold gas stream of a Nonius Kappa CCD (**1**, **2**·2THF, and **4**) or in a Bruker APEX-II CCD diffractometer (**3**) equipped with an Oxford Instruments low-temperature attachment. Data were collected using monochromated Mo Kα radiation (λ = 0.71073 Å). Scan type: ω and ϕ. Absorption corrections: semi-empirical (based on multiple scans). The structures were solved by Patterson (**1** and **3**) or direct methods (**2**·2THF) and refined on F^2 using the program SHELXL-97.[25] All non-hydrogen atoms were refined anisotropically. Hydrogen atoms were included using a riding model. Further details of the data collection and refinement are given in Table S1. Selected bond lengths and angles are collected in Tables 1−3; the crystal structures of complexes **1**, **2**·2THF, and **3** appear in Figures 1−3.

X-ray powder diffraction patterns were obtained at room temperature using a Rigaku D/max 2500 rotating anode generator by using graphite-monochromated Cu K radiation operating at 60 kV and 300 mA. Powder diffraction patterns were collected between 2θ of 3° and 50° with a 2θ stepping angle of 0.03°.

Computational Details. Single point DFT and TD-DFT calculations and NBO analysis were carried out with Gaussian 09 program package[26] using the PBE functional.[27] Overlap populations between molecular fragments were calculated using the Gaussum program.[28] Geometry optimizations at the DFT level were carried with Turbomole version 6.4 program[29] using the PBE functional together with the D3 dispersion correction previously described by Grimme.[30]

For single point DFT and TD-DFT calculations the following basis set combinations were employed for the metals Au and Tl: the 19-VE and 21-VE pseudopotentials from Stuttgart and the corresponding basis sets augmented with two *f* polarization functions,[31] respectively. The rest of the atoms were treated with SVP basis sets.[32,33]

In the case of geometry optimizations, the def2-TZVP basis set and effective core potential (ECP) combinations were employed for the metals Au and Tl.[34] The rest of the atoms were treated with SVP basis sets.[32,33]

■ ASSOCIATED CONTENT

Ⓢ Supporting Information

The Supporting Information is available free of charge on the ACS Publications website at DOI: 10.1021/acs.inorgchem.7b02035.

Details of data collection and refinement for **1**, **2**·2THF, and **3**, selected bond lengths and angles for **1** and **2**·THF, XPD patterns for **1**−**4**, and experimental and computational photophysical results (PDF)

Accession Codes

CCDC 1548531−1548533 and 1560240−1560241 contain the supplementary crystallographic data for this paper. These data can be obtained free of charge via www.ccdc.cam.ac.uk/data_request/cif, or by emailing data_request@ccdc.cam.ac.uk, or by contacting The Cambridge Crystallographic Data Centre, 12 Union Road, Cambridge CB2 1EZ, UK; fax: +44 1223 336033.

■ AUTHOR INFORMATION

Corresponding Authors

*E-mail: lippolis@unica.it.
*E-mail: josemaria.lopez@unirioja.es.
*E-mail: m-elena.olmos@unirioja.es.

ORCID

José M. López-de-Luzuriaga: 0000-0001-5767-8734
Miguel Monge: 0000-0002-9672-8279

Notes

The authors declare no competing financial interest.

■ ACKNOWLEDGMENTS

M.N. and V.L. thank Fondazione di Sardegna and Regione Autonoma della Sardegna (Progetti Biennali di Ateneo-Annualità 2016) for financial support. M.N. thanks the Universitá degli Studi di Cagliari for a grant. R.D., J.M.L.-d.-L., M.M., and M.E.O. thank the D.G.I. MINECO/FEDER (Project No. CTQ2016-75816-C2-2-P (AEI/FEDER, UE)). R.D. acknowledges CAR for a FPI grant. We also thank Centro de Supercomputación de Galicia (CESGA) for computing support.

■ REFERENCES

(1) (a) Pyykkö, P. Strong Closed-Shell Interactions in Inorganic Chemistry. *Chem. Rev.* **1997**, *97*, 597−636. (b) Pyykkö, P. Theoretical Chemistry of Gold. *Angew. Chem., Int. Ed.* **2004**, *43*, 4412−4456. (c) Pyykkö, P. Theoretical chemistry of gold II. *Inorg. Chim. Acta* **2005**, *358*, 4113−4130. (d) Pyykkö, P. Theoretical chemistry of gold III. *Chem. Soc. Rev.* **2008**, *37*, 1967−1997.

(2) (a) Forward, J. M.; Fackler, J. P.; Assefa, Z. In *Optoelectronic Properties of Inorganic Compounds*; Roundhill, D. M., Fackler, J. P., Jr., Eds.; Plenum: New York, 1999; pp 195−226. (b) López-de-Luzuriaga, J. M. In *Modern Supramolecular Gold Chemistry*; Laguna, A., Ed.; Wiley-VCH: Weinheim, 2008; p 347. (c) Fernández, E. J.; Laguna, A.; López-de-Luzuriaga, J. M. Luminescence in gold-heterometal complexes. *Gold Bull.* **2001**, *34*, 14−19 and references therein..

(3) (a) Fernández, E. J.; Laguna, A.; López-de-Luzuriaga, J. M.; Monge, M. Spanish Patent P200001391, 2003. (b) Fernández, E. J.;

DOI: 10.1021/acs.inorgchem.7b02035
Inorg. Chem. 2017, 56, 12551−12563

López-de-Luzuriaga, J. M.; Monge, M.; Olmos, M. E.; Pérez, J.; Laguna, A.; Mohamed, A. A.; Fackler, J. P., Jr. $\{Tl[Au(C_6Cl_5)_2]\}_n$: A Vapochromic Complex. *J. Am. Chem. Soc.* **2003**, *125*, 2022−2023. (c) Fernández, E. J.; López-de-Luzuriaga, J. M.; Monge, M.; Montiel, M.; Olmos, M. E.; Pérez, J.; Laguna, A.; Mendizábal, F.; Mohamed, A. A.; Fackler, J. P., Jr. A Detailed Study of the Vapochromic Behavior of $\{Tl[Au(C_6Cl_5)_2]\}_n$. *Inorg. Chem.* **2004**, *43*, 3573−3581. (d) Fernández, E. J.; López-de-Luzuriaga, J. M.; Monge, M.; Olmos, M. E.; Puelles, R. C.; Laguna, A.; Mohamed, A. A.; Fackler, J. P., Jr. Vapochromic Behavior of $\{Ag_2(Et_2O)_2[Au(C_6F_5)_2]_2\}_n$ with Volatile Organic Compounds. *Inorg. Chem.* **2008**, *47*, 8069−8076.

(4) Fernández, E. J.; Laguna, A.; López-de-Luzuriaga, J. M.; Monge, M.; Montiel, M.; Olmos, M. E.; Pérez, J. Thallium(I) Acetylacetonate as Building Blocks of Luminescent Supramolecular Architectures. *Organometallics* **2004**, *23*, 774−782.

(5) (a) Fernández, E. J.; López-de-Luzuriaga, J. M.; Olmos, M. E.; Pérez, J.; Laguna, A.; Lagunas, M. C. A Family of Au−Tl Loosely Bound Butterfly Clusters. *Inorg. Chem.* **2005**, *44*, 6012−6018. (b) Blake, A. J.; Donamaría, R.; Fernández, E. J.; Lasanta, T.; Lippolis, V.; López-de-Luzuriaga, J. M.; Manso, E.; Monge, M.; Olmos, M. E. Heterometallic gold(I)−thallium(I) compounds with crown thioethers. *Dalton Trans.* **2013**, *42*, 11559−11570. (c) Arca, M.; Donamaría, R.; Gimeno, M. C.; Lippolis, V.; López-de-Luzuriaga, J. M.; Manso, E.; Monge, M.; Olmos, M. E. 1,4-Bis(2′-pyridylethynyl)-benzene as a ligand in heteronuclear gold−thallium complexes. Influence of the ancillary ligands on their optical properties. *Dalton Trans.* **2015**, *44*, 6719−6730.

(6) Yam, V. W.-W.; Au, V. K.-M.; Leung, S. Y.-L. Light-Emitting Self-Assembled Materials Based on d^8 and d^{10} Transition Metal Complexes. *Chem. Rev.* **2015**, *115*, 7589−7728.

(7) (a) Fernández, E. J.; Laguna, A.; López-de-Luzuriaga, J. M.; Olmos, M. E.; Pérez, J. Gold−thallium supramolecular arrays with 4,4′-bipyridine. Solvent induction of luminescent networks. *Dalton Trans.* **2004**, 1801−1806. (b) Fernández, E. J.; Garau, A.; Laguna, A.; Lasanta, T.; Lippolis, V.; López-de-Luzuriaga, J. M.; Montiel, M.; Olmos, M. E. Long-Chain Ketimine Synthesis in a Gold−Thallium Polymer. *Organometallics* **2010**, *29*, 2951−2959. (c) Fernández, E. J.; Jones, P. G.; Laguna, A.; López-de-Luzuriaga, J. M.; Monge, M.; Olmos, M. E.; Pérez, J. Luminescent Gold(I)-Thallium(I) Arrays through N-Bidentate Building Blocks. *Z. Naturforsch.* **2004**, *59b*, 1379−1386.

(8) (a) Fernández, E. J.; Jones, P. G.; Laguna, A.; López-de-Luzuriaga, J. M.; Monge, M.; Pérez, J.; Olmos, M. E. Synthesis, Structure, and Photophysical Studies of Luminescent Two- and Three-Dimensional Gold−Thallium Supramolecular Arrays. *Inorg. Chem.* **2002**, *41*, 1056−1063. (b) Fernández, E. J.; Laguna, A.; López-de-Luzuriaga, J. M.; Monge, M.; Montiel, M.; Olmos, M. E.; Pérez, J. Thallium(I) Acetylacetonate as Building Blocks of Luminescent Supramolecular Architectures. *Organometallics* **2004**, *23*, 774−782. (c) Fernández, E. J.; Laguna, A.; Lasanta, T.; López-de-Luzuriaga, J. M.; Montiel, M.; Olmos, M. E. 1,2-Dibromo- and 1,2-Diiodotetrafluorobenzene as Precursors of Anionic Homo- and Heterometallic Gold Complexes. *Organometallics* **2008**, *27*, 2971−2979.

(9) Usón, R.; Laguna, A.; Laguna, M.; Manzano, B. R.; Jones, P. G.; Sheldrick, G. M. Synthesis and reactivity of bimetallic Au−Ag polyfluorophenyl complexes; crystal and molecular structures of $[\{AuAg(C_6F_5)_2(SC_4H_8)\}_n]$ and $[\{AuAg(C_6F_5)_2(C_6H_6)\}_n]$. *J. Chem. Soc., Dalton Trans.* **1984**, 285−292.

(10) Usón, R.; Laguna, A.; Laguna, M.; Manzano, B. R.; Tapia, A. Bimetallic gold—silver pentachlorophenyl complexes. *Inorg. Chim. Acta* **1985**, *101*, 151−153.

(11) Catalano, V. J.; Malwitz, M. A. Mixed-Metal Metallocryptands. Short Metal−Metal Separations Strengthened by a Dipolar Interaction. *J. Am. Chem. Soc.* **2004**, *126*, 6560−6651.

(12) Wieghardt, K.; Kleine-Boymann, M.; Nuber, B.; Weiss, J. Complexes of thallium(I) and -(III) containing 1,4,7-triazacyclononane (L) ligands. Kinetics and mechanism of the reduction of $[L_2Tl(III)]^{3+}$. Crystal structure of (N,N′,N″-trimethyl-1,4,7-triazacyclononane)thallium(I) hexafluorophosphate. *Inorg. Chem.* **1986**, *25*, 1309−1313.

(13) Heinzel, U.; Henke, A.; Mattes, R. Main-group and transition-metal complexes of1-thia-4,7-diazacyclononane, [9]aneN$_2$S. Crystal structures of$[VOCl_2([9]aneN_2S)]\cdot$ MeCN,$[Fe([9]aneN_2S)_2][ClO_4]_2$, $[Zn([9]aneN_2S)_2][PF_6]_2$,$[Ru(cym)([9]aneN_2S)][BPh_4]Cl_2\cdot$MeCN (cym = p-cymene),$[RhCl_3([9]aneN_2S)]\cdot H_2O$ and$[Tl([9]aneN_2S)][ClO_4]$. *J. Chem. Soc., Dalton Trans.* **1997**, 501−508.

(14) Blake, A. J.; Reid, G.; Schroder, M. Thallium macrocyclic chemistry: synthesis and crystal structures of $[Tl([18]aneN_2S_4)]PF_6$ and $[Tl([18]aneS_6)]PF_6$ ([18]aneN$_2$S$_4$= 1,4,10,13-tetrathia-7,16-diazacyclooctadecane, [18]aneS$_6$= 1,4,7,10,13,16-hexathiacyclooctadecane). *J. Chem. Soc., Dalton Trans.* **1992**, 2987−2992.

(15) Blake, A. J.; Greig, J. A.; Schroder, M. Notes. Thallium thioether chemistry. Synthesis and crystal structure of $[Tl([9]aneS_3)]PF_6$([9]aneS$_3$= 1,4,7-trithiacyclononane), showing infinite helices of $[Tl([9]aneS_3)]^+$ fragments. *J. Chem. Soc., Dalton Trans.* **1991**, 529−532.

(16) Blake, A. J.; Fenske, D.; Li, W.-S.; Lippolis, V.; Schroder, M. Cadmium(II), bismuth(III), lead(II) and thallium(I) crown thioether chemistry: synthesis and crystal structures of $[(CdI_2)_2([24]aneS_8)]$, $[(BiCl_3)_2([24]aneS_8)]$, $[Pb_2([28]aneS_8)][ClO_4]_4$ and $[Tl([24]aneS_8)]PF_6$ ([24]aneS$_8$ = 1,4,7,10,13,16,19,22-octathiacyclotetracosane; [28]aneS$_8$ = 1,4,8,11,15,18,22,25-octathiacyclooctacosane). *J. Chem. Soc., Dalton Trans.* **1998**, 3961−3968.

(17) Fernández, E. J.; López-de-Luzuriaga, J. M.; Monge, M.; Olmos, M. E.; Pérez, J.; Laguna, A. $[Au_2Tl_2(C_6Cl_5)_4]\cdot(CH_3)_2CO$: A Luminescent Loosely Bound Butterfly Cluster with a Tl(I)−Tl(I) Interaction. *J. Am. Chem. Soc.* **2002**, *124*, 5942−5943.

(18) Larson, L. J.; McCauley, E. M.; Weissbart, B.; Tinti, D. J. Luminescent Gold(I) Complexes. Optical and ODMR Studies of Mononuclear Halo(triphenylphosphine)- and Halo(triphenylarsine)-gold(I) Complexes. *J. Phys. Chem.* **1995**, *99*, 7218−7226.

(19) (a) Hsu, C. W.; Lin, C. C.; Chung, M. W.; Chi, Y.; Lee, G. H.; Chou, P. T.; Chang, C. H.; Chen, P. Y. Systematic investigation of metal-structure-photophysics relationship of emissive d10-complexes of group 11 elements: the prospect of application in organic light emitting devices. *J. Am. Chem. Soc.* **2011**, *133*, 12085−12099. (b) Rodriguez, L.; Ferrer, M.; Crehuet, R.; Anglada, J.; Lima, J. C. Correlation between photophysical parameters and gold-gold distances in gold(I) (4-pyridyl)ethynyl complexes. *Inorg. Chem.* **2012**, *51*, 7636−7641. (c) Ming Tong, G. S.; Chan, K. T.; Chang, X.; Che, C. M. Theoretical studies on the phoropsical properties of luminescent pincer gold(III) arylacetylide complexes: the role of π-conjugation at the C-deprotonated [ĈN̂C] ligand. *Chem. Sci.* **2015**, *6*, 3026−3037. (d) Gavara, R.; Lima, J. C.; Rodriguez, L. Effect of solvent polarity on the spectroscopic properties of an alkynyl gold(I) gelator. The particular case of water. *Photochem. Photobiol. Sci.* **2016**, *15*, 635−643.

(20) Hobbollahi, E.; List, M.; Hupp, B.; Mohr, F.; Berger, R. J. F.; Steffen, A.; Monkowius, U. Highly efficient cold-white light emission in a $[Au_2CuCl_2(P\cap N)_2]PF_6$ type salt. *Dalton Transactions* **2017**, *46*, 3438−3442 and references therein.

(21) (a) Donamaría, R.; Gimeno, M. C.; Lippolis, V.; López-de-Luzuriaga, J. M.; Monge, M.; Olmos, M. E. Tuning the Luminescent Properties of a Ag/Au Tetranuclear Complex Featuring Metallophilic Interactions via Solvent-Dependent Structural Isomerization. *Inorg. Chem.* **2016**, *55*, 11299−11310. (b) Wang, S.; Garzon, G.; King, C.; Wang, J. C.; Fackler, J. P., Jr. Luminescent extended one-dimensional heterobimetallic chain compounds with relativistic metal-metal bonds. Synthesis, crystal structures, and spectroscopic studies of $AuTl(MTP)_2$ and $Au_2Pb(MTP)_4$ (MTP = $[CH_2P(S)Ph_2]^-$). *Inorg. Chem.* **1989**, *28*, 4623−4629. (c) Wrighton, M.; Morse, D. L. Nature of the lowest excited state in tricarbonylchloro-1,10-phenanthrolinerhenium(I) and related complexes. *J. Am. Chem. Soc.* **1974**, *96*, 998−1003. (d) Itokazu, M. K.; Polo, A. S.; Murakami Iha, N. Y. Luminescent rigidochromism of *fac*-$[Re(CO)_3(phen)(cis\text{-}bpe)]^+$ and its binuclear complex as photosensors. *J. J. Photochem. Photobiol., A* **2003**, *160*, 27−32.

(22) Mudring, A.-V.; Rieger, F. Lone Pair Effect in Thallium(I) Macrocyclic Compounds. *Inorg. Chem.* **2005**, *44*, 6240−6243.

DOI: 10.1021/acs.inorgchem.7b02035
Inorg. Chem. 2017, 56, 12551−12563

(23) van de Water, L. G. A.; Buijs, W.; Driessen, W. L.; Reedijk, J. Correlation between the reactivities and the computed conformational and electronic properties of N,S,O-mixed-donor crown ethers. *New J. Chem.* **2001**, *25*, 243−249.
(24) Siegfried, L.; Kaden, T. A. Metal complexes with macrocyclic ligands. Part XIX. Synthesis and Cu^{2+} complexes of a series of 12-, 14- and 16-membered *cis*- and *trans*-N_2S_2-macrocycles. *Helv. Chim. Acta* **1984**, *67*, 29−38.
(25) Sheldrick, G. M. *SHELXL97, Program for Crystal Structure Refinement*; University of Göttingen: Germany, 1997.
(26) Frisch, M. J.; Trucks, G. W.; Schlegel, H. B.; Scuseria, G. E.; Robb, M. A.; Cheeseman, J. R.; Scalmani, G.; Barone, V.; Mennucci, B.; Petersson, G. A.; Nakatsuji, H.; Caricato, M.; Li, X.; Hratchian, H. P.; Izmaylov, A. F.; Bloino, J.; Zheng, G.; Sonnenberg, J. L.; Hada, M.; Ehara, M.; Toyota, K.; Fukuda, R.; Hasegawa, J.; Ishida, M.; Nakajima, T.; Honda, Y.; Kitao, O.; Nakai, H.; Vreven, T.; Montgomery, J. A., Jr.; Peralta, J. E.; Ogliaro, F.; Bearpark, M.; Heyd, J. J.; Brothers, E.; Kudin, K. N.; Staroverov, V. N.; Kobayashi, R.; Normand, J.; Raghavachari, K.; Rendell, A.; Burant, J. C.; Iyengar, S. S.; Tomasi, J.; Cossi, M.; Rega, N.; Millam, J. M.; Klene, M.; Knox, J. E.; Cross, J. B.; Bakken, V.; Adamo, C.; Jaramillo, J.; Gomperts, R.; Stratmann, R. E.; Yazyev, O.; Austin, A. J.; Cammi, R.; Pomelli, C.; Ochterski, J. W.; Martin, R. L.; Morokuma, K.; Zakrzewski, V. G.; Voth, G. A.; Salvador, P.; Dannenberg, J. J.; Dapprich, S.; Daniels, A. D.; Farkas, Ö.; Foresman, J. B.; Ortiz, J. V.; Cioslowski, J.; Fox, D. J. *Gaussian 09, Revision A.1*; Gaussian, Inc.: Wallingford, CT, 2009.
(27) Adamo, C.; Barone, V. Toward reliable density functional methods without adjustable parameters: The PBE0 model. *J. Chem. Phys.* **1999**, *110*, 6158−6171.
(28) O'Boyle, N. M.; Tenderholt, A. L.; Langner, K. M. A library for package-independent computational chemistry algorithms. *J. Comput. Chem.* **2008**, *29*, 839−845.
(29) Ahlrichs, R.; Bär, M.; Häser, M.; Horn, H.; Kölmel, C. Electronic structure calculations on workstation computers: The program system Turbomole. *Chem. Phys. Lett.* **1989**, *162*, 165−169.
(30) Grimme, S.; Antony, J.; Ehrlich, S.; Krieg, H. A consistent and accurate ab initio parametrization of density functional dispersion correction (DFT-D) for the 94 elements H-Pu. *J. Chem. Phys.* **2010**, *132*, 154104−154107.
(31) Andrae, D.; Haeussermann, U.; Dolg, M.; Stoll, H.; Preuss, H. Energy-adjusted ab initio pseudopotentials for the second and third row transition elements. *Theor. Chim. Acta* **1990**, *77*, 123−141.
(32) Schäfer, A.; Horn, H.; Ahlrichs, R. Fully optimized contracted Gaussian basis sets for atoms Li to Kr. *J. Chem. Phys.* **1992**, *97*, 2571−2578.
(33) Schäfer, A.; Huber, C.; Ahlrichs, R. Fully optimized contracted Gaussian basis sets of triple zeta valence quality for atoms Li to Kr. *J. Chem. Phys.* **1994**, *100*, 5829−5835.
(34) Weigend, F.; Ahlrichs, R. Balanced basis sets of split valence, triple zeta valence and quadruple zeta valence quality for H to Rn: Design and assessment of accuracy. *Phys. Chem. Chem. Phys.* **2005**, *7*, 3297−3305.

DOI: 10.1021/acs.inorgchem.7b02035
Inorg. Chem. 2017, 56, 12551−12563